



Research Article

Femtosecond nonlinear absorption and optical limiting action in nanoplatelet CuFe_2O_4 -decorated rGO nanocomposites

T. C. Sabari Girisun¹ · M. Saravanan¹ · S. Venugopal Rao²

© Springer Nature Switzerland AG 2019

Abstract

Using 800 nm infrared, 150 femtosecond (fs), 80 MHz high repetition rate laser pulse excitation, intensity-dependent ($I_0 = 245\text{--}735 \text{ MW/cm}^2$) measurements on the nonlinear absorption of copper ferrite hetero-architecture functionalized with three rGO contents (15, 25 and 40 wt%) were performed. Copper ferrite-rGO nanocomposite demonstrated a peculiar W-pattern [a peak (saturable absorption) with two valleys [reverse saturable absorption (RSA)] at extreme] in the open aperture Z-scan data for the decorated (15 wt%) rGO systems recorded at a low peak intensity ($I_0 = 245 \text{ MW/cm}^2$). The Z-scan traces were dominated by RSA characteristics due to two-photon absorption process at high peak intensities. The variation in intensity-dependent nonlinear absorption coefficient and ground-state absorption at laser excitation wavelength revealed the presence of excited-state absorption (ESA). The maximum two-photon absorption coefficient was recorded for CuFe_2O_4 -(40 wt%) rGO at 735 MW/cm^2 excitation, which is attributed to the combined contribution of rGO and CuFe_2O_4 that is four times higher than pure rGO and CuFe_2O_4 . The presence of layer like CuFe_2O_4 nanoplatelets upon the layer-structured rGO offers an added advantage in enhancing the nonlinear absorption coefficient. Near-resonant ESA-based optical limiters comprising CuFe_2O_4 -rGO can possibly be used as a versatile optical limiting material for eye safety against intense, high repetition rate fs laser pulses.

Keywords Reduced graphene oxide · Nonlinear absorption · Nonlinear refraction · Optical limiting

1 Introduction

Lasers these days are unavoidable tools in cutting edge technologies such as optics/photonics, and in particular, intense, femtosecond (fs)/picosecond (ps) laser pulses are in high demand in automobile, micro-fabrication and ultrafast measurement areas [1–7]. Such fs lasers, with capacity of delivering high intensities at short intervals of time, are capable of damaging the optical components, and therefore, numerous attempts are being made in preventing these laser-based accidents damaging the human eyes and precious sensors. The desideratum of ideal optical power limiters to delicate optical components (including the human eyes) with a low damage threshold due to

deliberate or unintentional exposure to these high power lasers is one of the ultimate challenges for the optics community [8–11]. Consequently, the development of optical limiting devices has shown tremendous advancement due to its possible utility in photonic application like laser safety devices, optical shutter, pulse shaping and light stabilizing sources [12–14]. However, the development of such materials (transparent at low intensity and translucent at high intensity) in ultrashort (fs) pulse time scale is still a work in progress. Several nonlinear mechanisms such as nonlinear absorption (NLA), nonlinear refraction (NLR) and nonlinear scattering (NLS) have been studied extensively in a variety of materials and have been engaged for achieving superior optical limiters [15, 16].

✉ T. C. Sabari Girisun, sabariirisun@bdu.ac.in; S. Venugopal Rao, soma_venu@uohyd.ac.in | ¹Nanophotonics Laboratory, Department of Physics, Bharathidasan University, Tiruchirappalli 620024, India. ²Advanced Centre of Research in High Energy Materials (ACRHEM), University of Hyderabad, Hyderabad, Telangana 500046, India.



SN Applied Sciences (2019) 1:400 | <https://doi.org/10.1007/s42452-019-0408-5>

Received: 5 February 2019 / Accepted: 25 March 2019 / Published online: 4 April 2019

Among these diverse phenomena, materials that possess nonlinear absorption can yield effective energy-absorbing optical limiter for various laser pulses. Since the intensity-dependent NLA measurements can provide additional information on the nature of nonlinear absorption, Z-scan experiments with different input intensities of excitation were performed to measure the nonlinear transmissivity of the sample. Graphene possesses interesting nonlinear absorption and refraction properties because of the interband transitions that are independent of the broad wavelength. To improvise the nonlinearity with tunability, graphene oxides (cheaper alternates of graphene) are often decorated with noble metal atom, porphyrin, phthalocyanine or covalent functionalization groups [17–20]. The remarkable light absorption and broad band emission of oxide derivatives of graphene (GO—graphene oxide, rGO—reduced graphene oxide) due to extended π -conjugate system have shown significant interest in laser damage protecting units. Here, the sp^2 hybridization from oxygen-containing groups left out after exfoliation varies which leads to change in NLO properties of rGO. Also, these residual functional groups upon the surface of rGO prevent aggregation and percolate various metal oxides such as Fe_2O_3 , $ZnFe_2O_4$, TiO_2 , ZnO and BBO [21–25]. Extensive efforts by various research groups have been extended toward understanding the nonlinear optical (NLO) properties of carbon-based graphene and graphene nanocomposites like graphene/epoxy resin [26], carbon black/epoxy resin [27], functionalized graphene fluoride [28], graphene families [29], graphene oxide [30], cobalt phthalocyanine [31], layered GO [32], polymer–GO [33], GO– Fe_2O_3 [21] and graphene [34]. Most of these materials have demonstrated superior NLO coefficients, which is essential for photonic applications. Particularly, metals incorporated in graphene nanocomposites depict impressive NLO and optical limiting performance owing to the combination of different mechanisms. Among metal oxide loading, ferrite stands high and recent work on ferrite-decorated rGO showed remarkable ultrafast nonlinearity characteristics. With intensity-dependent high repetition rate fs laser excitation, $CdFe_2O_4$ –rGO nanocomposite illustrated a shifting of RSA to SA because of the involvement of various molecules with respect to excitation intensity [35]. Impressed by this factor, we have extended our earlier investigations on ferrite-decorated rGO systems. Earlier reports showcase that the combination of rGO with $CuFe_2O_4$ can yield potential systems with strong nonlinearity [36]. Also ferrites are investigated in different optoelectronic applications as it possess the advantages of (a) owning $3d^{10} 4s^1$ configuration in the valence shell, (b) available at low cost and (c) environmentally benign [37–39]. So using the different intensities ($I_0 = 245, 490$ and 735 MW/cm^2) of Ti:Sapphire (150 fs, 800 nm and 80 MHz)

laser pulses, NLO activities of a series of $CuFe_2O_4$ –rGO nanocomposites were measured. It is well known that inclusion of copper ferrite can induce excited states near the excitation wavelength, and thus, there is a possibility to demonstrate ESA-based optical limiters. Therefore, the motivation of the work is to demonstrate a near-resonant excited-state absorption-based optical limiter comprising $CuFe_2O_4$ –rGO with improved NLO performance for eye safety against intense, high repetition rate fs laser pulses. Interesting transition of nonlinear absorption mechanism (SA, W-pattern, sequential 2PA) with respect to the composition of samples was observed. Thus, the basic of understanding the influence of elemental composition (Cu) and morphology in altering the nonlinear optical performance of the material is analyzed.

2 Experimental details

2.1 Preparation of solar exfoliated reduced graphene oxide

Reduced graphene oxide (rGO) that resembles the internal structure of graphene is chosen as host element since graphene is expensive to be produced in bulk quantities. Using inexpensive graphite as a starting precursor, graphene oxide was prepared by modified Hummer's method [40]. The process of oxidation was achieved by reacting graphite (1 g, Alfa Aesar) with sodium nitrate (1 g, EMPLURA) in the presence of sulfuric acid (4 ml). The process of oxidation was continued by the addition of potassium permanganate (6 g, EMPLURA), and the reaction being exothermic excess of heat was released. The solution was immersed in ice bath to control the temperature well below 20°C . Hydrogen peroxide (6 ml) hydrated solution was used to terminate the oxidation process, and the obtained black powder was washed (with HCl and H_2O), centrifuged (8000 rpm, 10 min) and dried (60°C , 12 h). The best way to remove the attached functional groups without destructing the layered structure of graphene is to reduce graphite oxide using solar radiation. The process of exfoliation was activated by focusing solar radiation upon prepared graphene oxide using convex lens of focal length 100 cm. The transition of light brown to dark black accompanied by the sudden increase in the volume ascertains the formation of solar exfoliated reduced graphene oxide [41]. Here the process of de-oxygenation in graphene oxide occurred due to localized thermal excitation (150 – 200°C in 1–2 s) arising from the photoacoustic effect originated through focused solar radiation.

2.2 Preparation of CuFe_2O_4 -rGO nanocomposite

The decoration of copper ferrite with different load contents upon reduced graphene oxide to form CuFe_2O_4 -rGO nanocomposites was achieved by a one-step hydrothermal method. Here, nitrates of copper and ferric (1:2 molar ratio) were used as precursor to form CuFe_2O_4 . Upon reduced graphene oxide (rGO) with various contents (15, 25 and 40 wt%), copper ferrite metal oxide was formed. The oxygen functionalities on rGO sheets serve as nucleation sites to accommodate copper and ferrous oxides dissociating from the respective nitrates and thus forming CuFe_2O_4 -rGO nanocomposites. The reaction was carried out in an autoclave unit (volume of 150 mL) with rGO dispersed metal nitrate solutions being heated at 180 °C under ambient pressure. Solvable byproducts in the precipitate were removed with water washing and then dried in air atmosphere (60 °C, 24 h). The above procedure was carried out for 0, 15, 25, 40 wt% of rGO to attain pure CuFe_2O_4 nanoparticles and CuFe_2O_4 -rGO nanocomposites.

2.3 Z-scan experiment

Open aperture Z-scan experiments were carried out on CuFe_2O_4 -(15, 25 and 40 wt%) rGO nanocomposite to study the nonlinear absorption at various input intensities. An excitation source of Ti:Sapphire laser oscillator (Chameleon, M/s Coherent) was used providing output at a wavelength of 800 nm, pulses with duration of 150 fs at 80 MHz repetition rate. The laser pulses were focused using 100-mm focus lens, and the corresponding beam waist was estimated to be $\sim 25.5 \mu\text{m}$ at 800 nm, and all the experiments were performed with various input peak intensities (245–735 MW/cm^2). From the recorded open aperture Z-scan data, the variation in normalized transmittance with respect to light fluence $[F(z)]$ was derived using standard relations [22].

3 Results and discussion

3.1 Preliminary confirmation and structural studies

Recorded XPS patterns of pristine and decorated GO are illustrated in Fig. 1a. For rGO, peaks that represent carbon (285.3 eV) and oxygen (529.7 eV) environment of the molecule are shown in Fig. 1a. C 1s XPS (Fig. 1b) pattern of reduced graphene oxide has peaks at 284.5 eV (C=C), 285.8 eV (C–O) and 288.6 eV (C=O) which represents different functional groups of reduced graphene oxide. The wide-scan XPS spectrum of CuFe_2O_4 -(15 wt%) rGO nanocomposite obviously depicts the characteristic peaks at 285.01 eV, 532.83 eV, 722.99 eV, 710.10 eV and 932.80 eV,

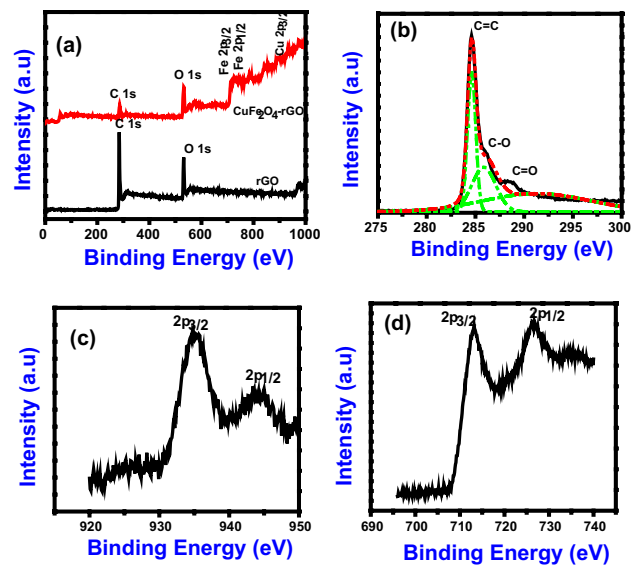


Fig. 1 XPS spectra of **a** rGO and CuFe_2O_4 -(15 wt%) rGO nanocomposites, **b** C 1s XPS spectra of rGO and **c** Cu 2p, **d** Fe 2p core-level spectrum of CuFe_2O_4 -(15 wt%) rGO nanocomposites. The peaks in **b** were fitted with Gaussian curves, and the green lines represent the components of Gaussian fit made on C 1s XPS spectrum

corresponding to the binding energy of C 1s, O 1s, Fe 2p and Cu 2p, respectively. Figure 1c (Fe) and Fig. 1d (Cu) represent the core-level XPS pattern for composite. Peaks at binding energies of 713.10 eV (Fe $2p_{1/2}$), 718.3 eV (Fe^{3+}), 726.14 eV (Fe $2p_{1/2}$), 935.11 (Cu $2p_{3/2}$) and 944.25 eV (Cu $2p_{1/2}$) ensure the presence of metals (copper and ferrous) ions in the composite which is found to match well with the literature [42, 43].

X-ray diffraction patterns were recorded to confirm the formation of the support as well as the composite, and data are shown in Fig. 2. In the XRD of GO, the disappearance of graphite diffraction peak ($2\theta = 26^\circ$) and the formation of characteristic peak at lower angle ($2\theta = 10.6^\circ$) confirm the complete oxidation during Hummer's method [22]. The expected reverse observation (graphene oxide turning themselves as graphene like structure) of no diffraction at lower angle and broad weak XRD peak at 24° that corresponds to (002) plane of rGO was observed in solar exfoliated product. For CuFe_2O_4 -decorated rGO hetero-architecture, the presence of (200), (211), (422), (004), (312) and (224) reflection planes was ascribed to the tetragonal structure of CuFe_2O_4 [JCPDS: 34-0425]. In the CuFe_2O_4 -rGO hetero-architecture, exfoliation of rGO occurred because of crystal growth of copper ferrite between the rGO sheets. In the recorded FTIR spectrum (Fig. 3), rGO shows broad vibrational band due to the stretching mode of hydroxyl groups (3420 cm^{-1}). Upon decoration, rGO shows a decrease in absorption intensity of 3420 cm^{-1} (O–H), 1725 cm^{-1} (C=O) and 1120 cm^{-1}

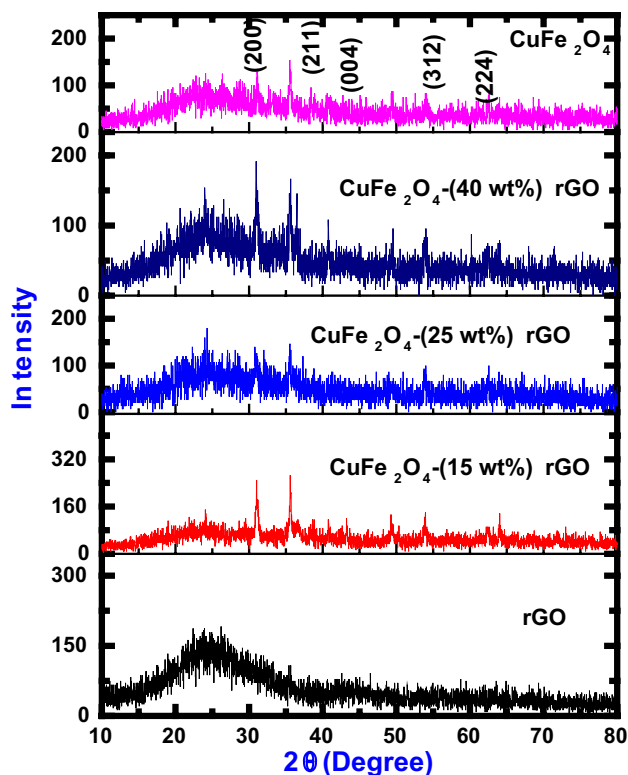


Fig. 2 XRD patterns of pure and decorated CuFe_2O_4 -rGO composites

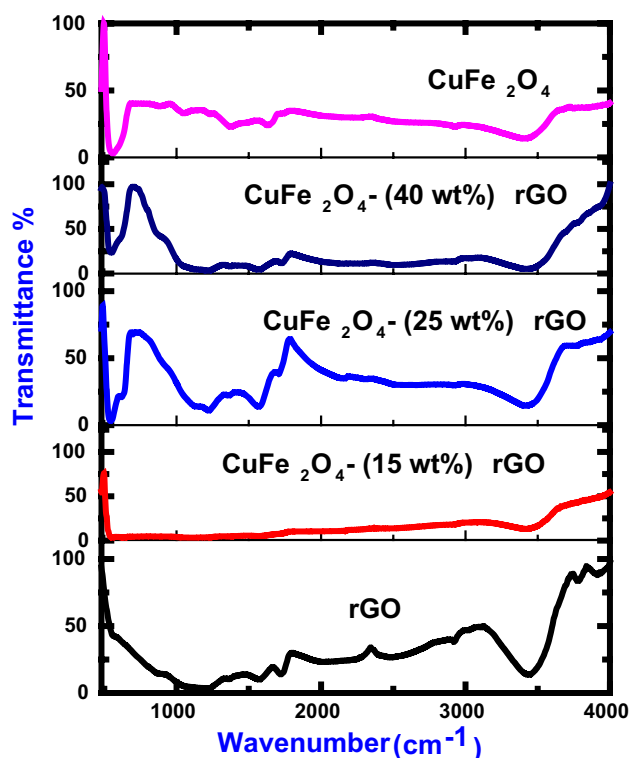


Fig. 3 Recorded FTIR of rGO, CuFe_2O_4 -(15 wt%) rGO, CuFe_2O_4 -(25 wt%) rGO, CuFe_2O_4 -(40 wt%) rGO and CuFe_2O_4

(C–O) which indicate that rGO was further reduced to a great extent during the incorporation of CuFe_2O_4 . New absorption bands observed at 545 cm^{-1} (Cu^{2+} stretching in the octahedral site) and 454 cm^{-1} (Fe^{3+} stretching in the tetrahedral site) belong to CuFe_2O_4 in the composite. For CuFe_2O_4 -(40 wt%) rGO sample, the FTIR spectrum showed peaks at 3427 cm^{-1} (O–H), 2928 cm^{-1} ($-\text{CH}_2$), 1726 cm^{-1} (C–O), 1620 cm^{-1} (C=C) and 1125 cm^{-1} (C–O), and in the case of (25 wt%) rGO, the peak at 2928 cm^{-1} ($-\text{CH}_2$) vanished for the nanocomposite. The effective removal of functional groups in CuFe_2O_4 -(15 wt%) rGO was observed as many of the functional groups almost vanished in the IR spectra of the composite.

Raman spectroscopy is an essential experimental technique for identifying the defects states formed during functionalization of graphene. In recorded Raman spectra with 532 nm laser excitation (Fig. 4) of copper ferrite functionalized upon three rGO contents (15, 25 and 40 wt%), G band (1598 cm^{-1} , 1598 cm^{-1} and 1590 cm^{-1}) and D band (1300 cm^{-1} , 1327 cm^{-1} and 1348 cm^{-1}) of graphene were observed. Because of the reduction, I_D/I_G reduces to 0.78 (rGO) which is smaller compared with 0.99 (GO). Also, the CuFe_2O_4 -rGO nanocomposite exhibited the characteristic CuFe_2O_4 Raman modes at 216, 281, 392 (E_{2g} and T_{2g}) and $597, 676\text{ cm}^{-1}$ (A_{1g}). And I_D/I_G ratio of

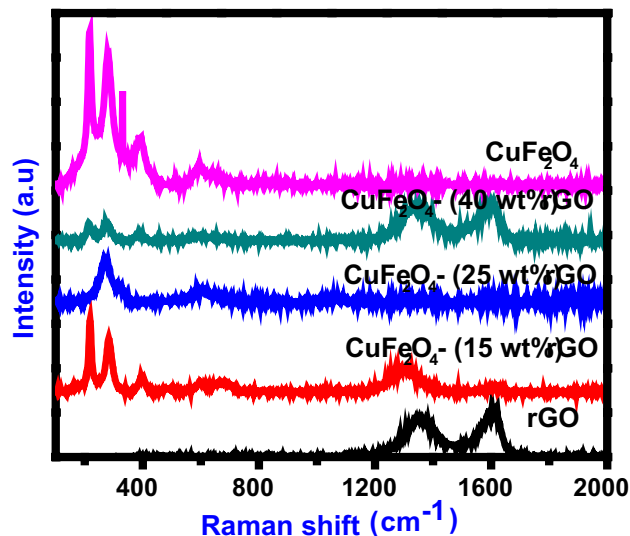


Fig. 4 Raman spectra of rGO, CuFe_2O_4 , CuFe_2O_4 -(15 wt%) rGO, CuFe_2O_4 -(25 wt%) rGO and CuFe_2O_4 -(40 wt%) rGO

nanocomposite was estimated to be 5.06, 1.07 and 0.91, which emphasis the dominance of structural defects in the composite that can result in variation in optical properties. The perfect graphene domain (L_a) which is inversely

proportional to I_D/I_G ratio was evaluated using the excitation energy (eV) by standard relation [44]. The crystallite sizes of CuFe_2O_4 -(15, 25 and 40 wt%) rGO were calculated to be 1.38 nm, 6.53 nm and 7.76 nm, respectively. In fact, the change in I_D/I_G ratio along with La value emphasis the removal of oxygen element organic groups and the incorporation of bond between CuFe_2O_4 and rGO sheets during hydrothermal reaction. Altogether, chemical state (XPS), crystal structure (XRD), molecular structural (FTIR) and defect state (Raman) analysis confirms the successful synthesis of CuFe_2O_4 -rGO nanocomposite through the hydrothermal treatment.

3.2 Textural, magnetic and linear optical properties

SEM and TEM techniques were used to analyze the structural morphology of rGO and CuFe_2O_4 -decorated rGO hetero-architectures, which inveterate the versatile morphology of CuFe_2O_4 -rGO nanostructures. It is manifesting to be observed that in rGO, exfoliated GO appears as transparent, ultrathin and distinguished sheets. Recorded SEM image (Fig. 5) showcases the existence of different morphologies for pure CuFe_2O_4 (clusters of platelets) and CuFe_2O_4 decorated upon 15 wt% rGO (spindle), 25 wt% rGO (aggregate of platelets and spindle) and 40 wt% rGO (well-distributed thin platelets). Here as graphene content

increases, the nucleation formed on the surface of sheets preferred the formation of platelets like structures of CuFe_2O_4 . TEM image (Fig. 6) of reduced graphene oxide illustrates curvy and wrinkled sheets of graphene attributed to solar exfoliation process. For pure CuFe_2O_4 , the formation of nanoplatelets with 23 nm width was observed. A uniform distribution of nanoplatelets and nanospindles of copper ferrite functionalized upon rGO contents (15, 25 and 40 wt%) with size 9 nm, 17 nm and $(67 \times 28 \text{ nm})$, respectively, was witnessed. The increase in graphene content leads to the increase in the number of nucleation sites of CuFe_2O_4 and provides a transformation in the morphology from platelets to spindle aided from protrusions expanding with growth. The magnetic property of CuFe_2O_4 nanoparticles and CuFe_2O_4 -rGO nanocomposite using a vibrating sample magnetometer (VSM) was investigated. Figure 7 illustrates the S-type curve (hysteresis loop) of room temperature magnetized (with an applied magnetic field) nanocomposite. Copper ferrite being the magnetization contributing entity, its size and morphology play a significant role in deciding the ordering and magnetization of the sample. The magnetic remanences of CuFe_2O_4 nanoparticles and CuFe_2O_4 -rGO composites were found to be in the range 10^{-6} emu/g which is nearly zero, suggesting its superparamagnetic behavior. Higher saturation magnetization and lower coercivity were observed

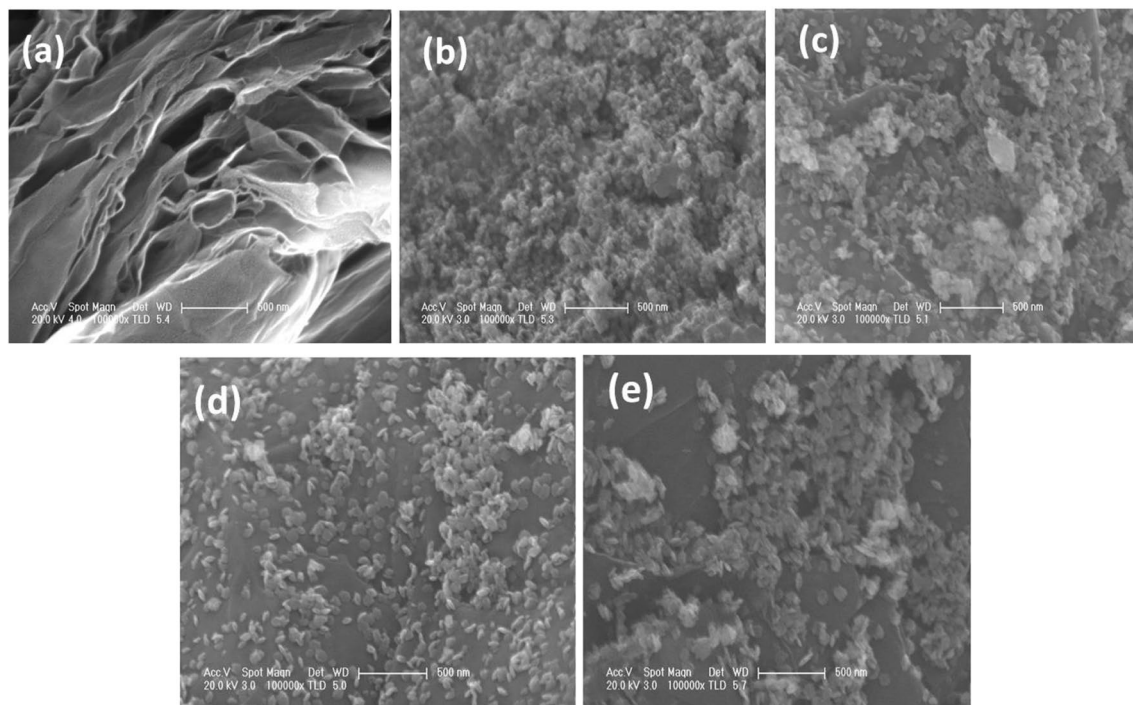


Fig. 5 SEM images of **a** rGO (layered structure), **b** CuFe_2O_4 (nanoplatelets), **c** CuFe_2O_4 -(40 wt%) rGO (nanoplatelets of copper ferrite upon rGO layers), **d** CuFe_2O_4 -(25 wt%) rGO (nanoplatelets of cop-

per ferrite upon rGO layers), **e** CuFe_2O_4 -(15 wt%) rGO (nanospindle of copper ferrite upon rGO layers)

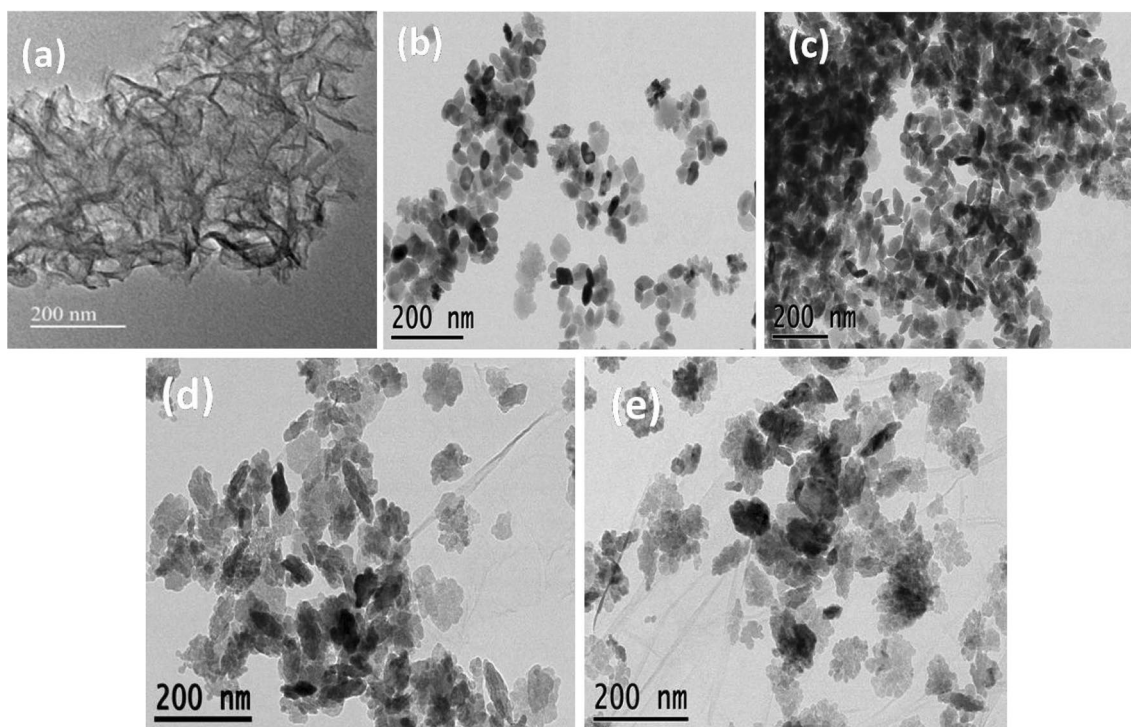


Fig. 6 TEM images of **a** rGO, **b** CuFe₂O₄, **c** CuFe₂O₄-(15 wt%) rGO, **d** CuFe₂O₄-(25 wt%) rGO, **e** CuFe₂O₄-(40 wt%) rGO nanocomposite

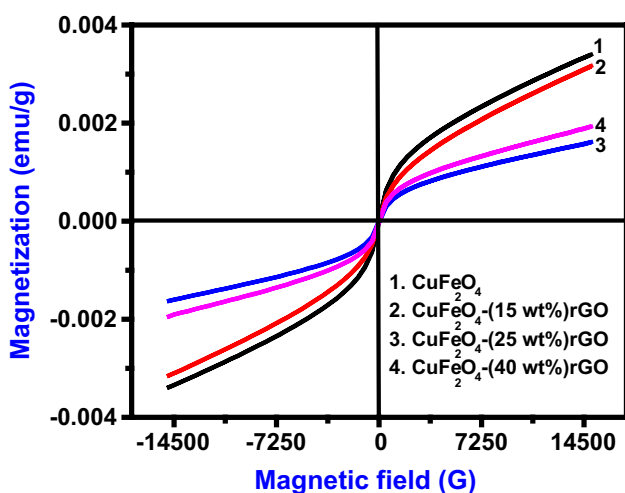


Fig. 7 Room temperature M-H curves of the pure CuFe₂O₄, CuFe₂O₄-(15 wt%) rGO, CuFe₂O₄-(25 wt%) rGO and CuFe₂O₄-(40 wt%) rGO nanocomposite

for pure copper ferrite (3.399×10^{-3} emu, 15.271 G) than for CuFe₂O₄-(40 wt%) rGO (1.624×10^{-3} emu, 35.150 G). It is be noted that saturation magnetization of CuFe₂O₄ decreases upon loading in rGO. Similar superparamagnetism with higher coercivity due to increased magnetocrystallinity was reported for Fe-Al₂O₃ system [35, 45, 46]. Copper ferrites when scaled down to nanometer regime

alter the surface/interface properties, electronic states and magnetic properties. Nanocomposites containing both magnetic and NLO properties can offer interactions between magnetic susceptibility and nonlinear absorption in the material, which can be utilized to realize magneto-controlled NLO materials. In such a case, by tuning the magnetic properties of the nanocomposites, the magnetic anisotropy of the magnetic ion at the interfaces can be reduced which leads to strong nonlinear optical response. Thus, with the application of external magnetic field it is possible to control the optical properties of the magnetic nanoparticles used in optical devices. Generally, the magneto-optical effect that transpires in magnetic fluids is believed to be the consequences of anisotropy in the dielectric constant (induced by the orientation of suspended particles). This induced anisotropy can also result in optical anisotropy either in the refractive index or absorbance or in both. A super paramagnetic behavior was observed mainly due to the contribution of copper ferrite nanoparticles, in which a fraction of Fe³⁺ is distributed out of the preferred octahedral A sites to tetrahedral B sites leading to the coupling between the cations. A larger extent of conjugation increases the chance for electron/energy transfer which leads to enhanced nonlinear optical response. Thus, functionalization of copper ferrite upon rGO has introduced the emergence of localized magnetic moment (super paramagnetic nature).

UV–visible absorbance data of the reduced graphene oxide, CuFe_2O_4 and CuFe_2O_4 -rGO nanocomposite are shown in Fig. 8. Upon reduction to rGO, the absorption maximum of GO was red shifted to 278 nm (238 nm) and 388 nm (290 nm). The absorptions of CuFe_2O_4 were observed at 445 nm (ligand field transitions) and 537 nm

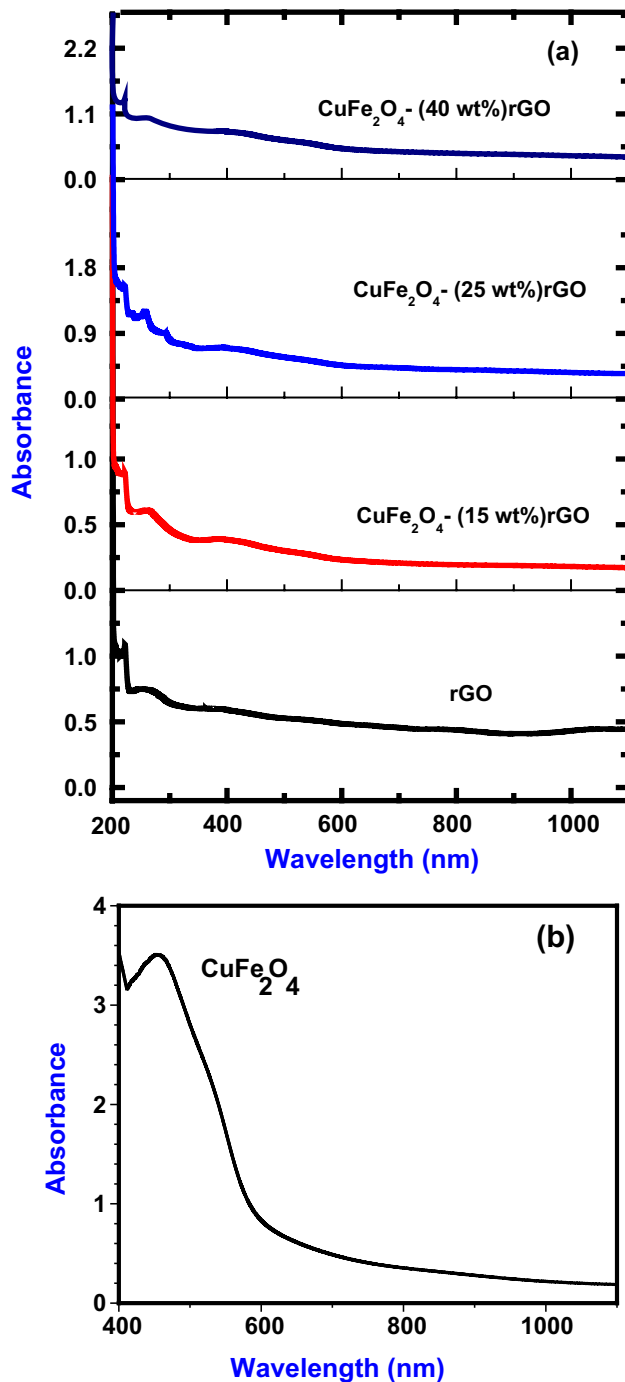


Fig. 8 UV–visible absorption spectra of **a** rGO, CuFe_2O_4 -(15 wt%) rGO, CuFe_2O_4 -(25 wt%) rGO, CuFe_2O_4 -(40 wt%) rGO and **b** pure CuFe_2O_4

(surface plasmon resonance (SPR), peak of Cu nanoparticle). The absorption peak of (CuFe_2O_4 -rGO nanocomposite) at 260 nm, 394 nm, 436 nm and 541 nm is the indicative of CuFe_2O_4 deposition on rGO nanosheets. Compared to CdFe_2O_4 -rGO nanocomposite [35], CuFe_2O_4 -rGO shows higher absorbance at the chosen wavelength of excitation (800 nm) which makes them possible to observe near-resonant nonlinearity.

3.3 Nonlinear refraction

It is known that the ground-state absorption and ESA together can induce intensity-dependent refractive index [16]. With high repetition rate intense IR laser pulses, it can be generally expected that NLR arises mainly due to thermal lensing effects. Here, since the closed aperture transmittance is affected by the nonlinear refraction and absorption, the determination of n_2 is less straight forward from the closed aperture scans. It is necessary to separate the effect of nonlinear refraction from that of nonlinear absorption. A simple and effective method [47] to obtain purely effective n_2 is to divide the closed aperture transmittance by the corresponding open aperture scans. Figure 9 presents the ratio of closed (CA) aperture by open aperture Z-scan profiles recorded with a peak intensity of 245 MW/cm^2 . Both pristine CuFe_2O_4 and CuFe_2O_4 functionalized upon (15, 25 and 40 wt%) rGO contents exhibit negative nonlinear refractive index-based self-defocusing nature. The value of n_2 was evaluated through theoretical fitting of closed aperture normalized transmittance

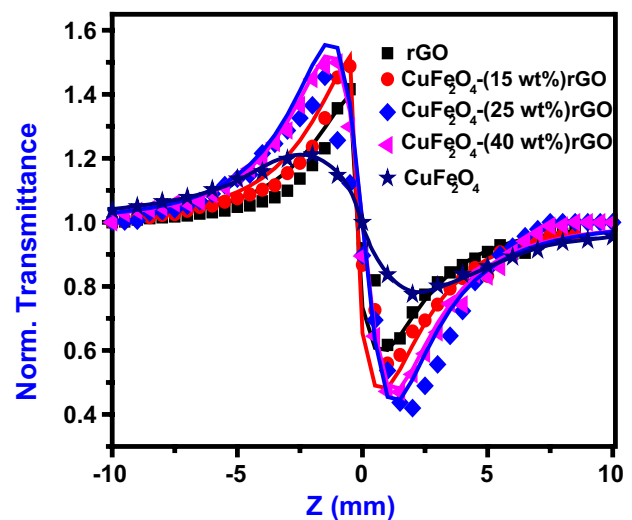


Fig. 9 CA Z-scan pattern of rGO, CuFe_2O_4 -(15, 25 and 40 wt%) rGO and CuFe_2O_4 at an intensity of 245 MW cm^{-2} of Ti:Sapphire (800 nm, 150 fs and 80 MHz) laser. The scattered circles represent the experimental data, and the solid line is the theoretical fit as proposed by Sheik-Bahae

(T_{CA}) [48]. As expected, pure rGO with its planar structure and capacity to dissipate heat quickly possesses stronger nonlinear refraction than pure CuFe_2O_4 . Here rGO ($-2.8 \times 10^{-16} \text{ m}^2/\text{W}$) possesses two times higher n_2 than CuFe_2O_4 ($-1.4 \times 10^{-16} \text{ m}^2/\text{W}$). In the CuFe_2O_4 -rGO nanocomposite, the increase in the content of graphene boosts the nonlinear refractive index. The nonlinear refractive index of CuFe_2O_4 - (15, 25 and 40 wt%) rGO nanocomposite was estimated to be -1.7 , -3.3 and $-3.8 \times 10^{-16} \text{ m}^2/\text{W}$. The π -electron distribution and the free carriers of the sp^2 domain in graphene sheets are the prime reason for the occurrence of NLR in rGO. Here excitation with ultrafast lasers on the sample leads to transfer of carriers in the NP's state. Enhancement in carrier density is observed in the composite system due to the low lifetime of the excited carriers from the NP's to the valence band of rGO leading to the improvement in NLR. Strong thermal conductivity due to the planar structure of rGO and high repetition rate fs laser excitation results in dominant thermal contribution and high n_2 . It is pertinent to note here that the excitation of the laser involves high repetition rate (80 MHz) which is much higher than the thermal diffusion time and there is a possibility that the cumulative thermal effects also contribute to the Z-scan signal. Excess energy from thermal dissipation redistributes within the solute molecules which turn them into intramolecular heat and may also further raise the solution temperature by dissipating eventually into the photon. Thus, the change of refractive index due to diffusion effect has considerable applications in optical communication systems that are operating at high repetition rate. As a result of the contribution of thermal nonlinearity, the NLO coefficients of the investigated materials were found to be higher than most of the earlier reports. Measurements with fs, kHz pulses will separate the thermal contribution, and these will be taken up in near future.

3.4 Intensity-dependent nonlinear absorption

Nonlinear optical absorption is broadly classified as two classes: Actual transitions give resonant nonlinearity which is slow and virtual transitions generate non-resonant nonlinearity that is fast in nature. Linear absorption is a predominant mechanism in the resonant region, while it is multi-photon processes in the non-resonant region. To understand the nonlinear absorption process of the prepared sample, the acquired data were fitted using the standard relation for open aperture normalized transmittance [49]. It is to be noted that the match found between numerical and experimental data just ascertains the reliability of the experiment performed and it does not confirm or indicate the occurrence of 2PA, to be genuine or sequential two-step ESA. Change

in the nonlinear absorption coefficient corresponding with input intensity can provide information on the mechanism involved. Genuine 2PA occurs when β -value remains constant for varied input intensity as weak 2PA cannot drain the population of electrons in the ground state. However, in ESA process due to substantial depletion of ground-state population nonlinear absorption coefficient either will increase or decrease as function of peak intensity. The OA data recorded for rGO and CuFe_2O_4 (Fig. 10a–f) show RSA pattern with minimum transmittance at the focus. As depicted in the linear absorption spectrum, materials possess small absorption in the domain of excitation wavelength, and hence, the observed nonlinearity is expected to be of resonant type. The changes in input intensity on the interaction with the material play an important role in 2PA process [50]. The measured data were found to be fitting well with the theoretical 2PA equation. The possible mechanisms for 2PA in such materials process are depicted in Fig. 11. Here, for pure rGO and CuFe_2O_4 2PA coefficient was found to be increasing with input peak intensity. This clearly suggests that the observed nonlinearity arises due to ESA process, i.e., $1\text{PA} + \text{ESA} = 2\text{PA}$. The source of the witnessed nonlinearity in rGO has occurred due to the process mentioned below: As witnessed in the ground-state (UV-Visible) absorption pattern of rGO and CuFe_2O_4 , the materials possess considerable absorption in excitation region (800 nm, 1.55 eV), and thus, the observed nonlinearity is of resonant type. Under NIR excitation (800 nm), electrons in the ground state absorb two photons (800 nm, 1.55 eV) through sequential process and transit to the excited state of rGO (388 nm, 3.2 eV) and pure copper ferrite (445 nm, 2.79 eV).

The OA pattern in Fig. 10b, c of the 15 wt% decorated system shows a combined SA and RSA pattern (W-pattern) for low input intensity ($I_0 = 245 \text{ MW cm}^{-2}$). The W-pattern with the 2PA process is formed due to the additional hump peak ($Z=0$) flanked between the two valleys representing SA peak. And the nonlinear absorption coefficient is affected by the existence of the two competing effects (RSA and SA). As the general open aperture equation for 2PA process cannot be modeled for W-type nonlinear absorption because of expected inhomogeneous broadening of transitions in these conditions, the 2PA coefficient is obtained by fitting the experimental data with following equations [51]

$$\beta(I) = \beta_{\text{RSA}}(I) + \beta_{\text{SA}}(I) = \frac{\beta_{\text{RSA}}}{1 + \frac{I}{I_{\text{S}}^{\text{RSA}}}} + \frac{\beta_{\text{SA}}}{1 + \frac{I}{I_{\text{S}}^{\text{SA}}}}$$

2PA coefficients obtained for the best fits to the experimental data are presented in Table 1. The experiments

Fig. 10 Intensity-dependent OA Z-scan curve of pure **a** rGO, **b** CuFe₂O₄-(15 wt%) rGO (245 MW/cm²), **c** CuFe₂O₄-(15 wt%) rGO (245–735 MW/cm²), **d** CuFe₂O₄-(25 wt%) rGO, **e** CuFe₂O₄-(40 wt%) rGO and **f** CuFe₂O₄. The experimental OA data (represented as scattered circles) were fitted (solid line) with the theoretical equations as proposed by Sheik Bahae

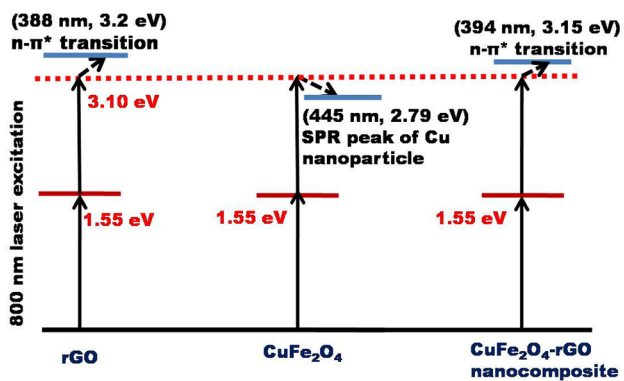
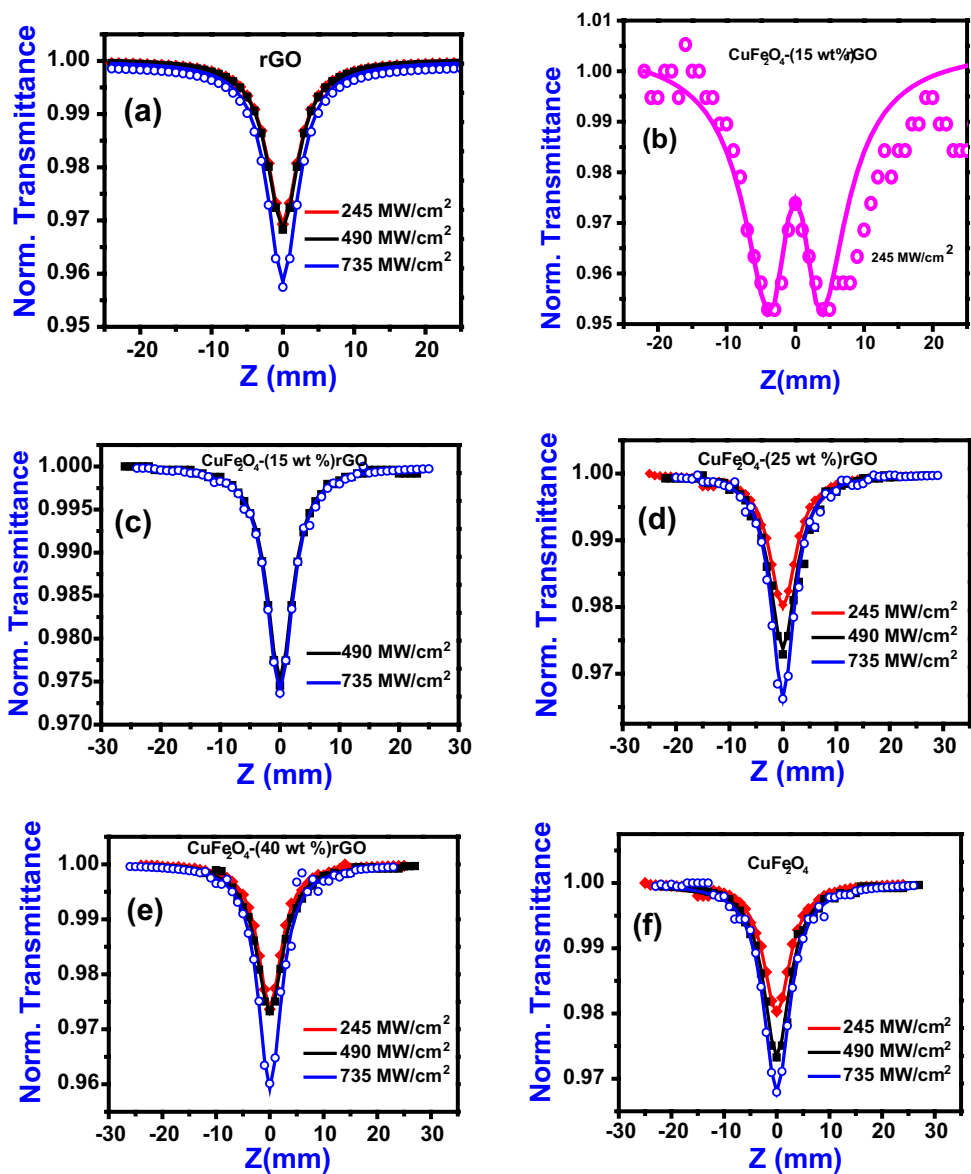


Fig. 11 Possible electronic transitions for observed 1PA + ESA = 2PA in pure and decorated systems. Here 2PA involves n-π* transition state of rGO and CuFe₂O₄-rGO nanocomposite and SPR peak of Cu nanoparticles for pure CuFe₂O₄

were performed on an automated Z-scan experimental setup. The errors in estimation of focal spot size, peak intensities, fitting procedures and calibration of intensity are major sources of error in the estimation of the NLO coefficients. Based on several measurements, the maximum error was estimated to be ± 5%. As the error correction is employed uniformly, the change in NLO coefficients of different samples was directly compared.

It is evident that since the sample shows negligible linear transmittance at 800 nm, the contribution of linear absorption coefficient (α_0) is neglected. The dominance of RSA pattern was observed for the higher excitation intensity, thus providing stronger 2PA coefficient, while for copper ferrite-decorated (25 wt% and 40 wt%) reduced graphene oxide systems it displayed RSA (valley) at lower input intensity ($I_0 = 245 \text{ MW cm}^{-2}$). Therefore, it can be

Table 1 Estimated nonlinear absorption coefficient and onset optical limiting threshold values

NLO parameters	800 nm, 150 fs, 80 MHz excitation					
	Nonlinear absorption coefficient (β_{2PA}) $\times 10^{-10}$ m/W			Onset optical limiting threshold ($\mu\text{J}/\text{cm}^2$)		
	$I_o = 245 \text{ MW}/\text{cm}^2$	$I_o = 490 \text{ MW}/\text{cm}^2$	$I_o = 735 \text{ MW}/\text{cm}^2$	$I_o = 245 \text{ MW}/\text{cm}^2$	$I_o = 490 \text{ MW}/\text{cm}^2$	$I_o = 735 \text{ MW}/\text{cm}^2$
rGO	2.1 ± 0.10	2.5 ± 0.12	2.7 ± 0.13	38.45	35.66	31.42
CuFe_2O_4	0.7 ± 0.03	1.0 ± 0.05	3.3 ± 0.16	57.50	54.12	27.53
CuFe_2O_4 -(15 wt%) rGO	0.17 ± 0.01	0.9 ± 0.04	1.1 ± 0.05	–	56.73	55.59
CuFe_2O_4 -(25 wt%) rGO	1.0 ± 0.05	1.4 ± 0.14	6.7 ± 0.33	57.50	45.22	22.29
CuFe_2O_4 -(40 wt%) rGO	1.3 ± 0.06	1.7 ± 1.70	12.7 ± 0.63	52.38	35.36	12.45

deduced that as the size of CuFe_2O_4 -rGO increases, the effect of RSA increased suppressing SA behavior. This might be due to greater cross section of excited states than ground state for larger particles. For all higher intensities ($I_o = 490 \text{ MW cm}^{-2}$ and 735 MW cm^{-2}), decorated rGO systems exhibited reverse saturable absorption. Here the prepared reduced graphene oxide contains both sp^2 (Pristine graphene honeycomb lattice) and sp^3 (defects state and oxygen-containing functional groups) hybridized domains. sp^3 hybridization in the carbon units of rGO leads to 2PA at different ($I_o = 245 \text{ MW cm}^{-2}$, $I_o = 490 \text{ MW cm}^{-2}$ and $I_o = 735 \text{ MW cm}^{-2}$) intensities provided by ultrafast pulses. It is to be mentioned that decorated systems depict linear absorption maxima at 394 nm due to $n-\pi^*$ transition in the rGO. As the composites possess energy states near to excitation wavelength, the resonant nonlinearity gives rise to sequential 2PA (two photons were sequentially absorbed) rather than genuine 2PA. The incorporation of CuFe_2O_4 on the rGO system results in the participation of σ -states (sp^3) in 2PA process. The increase in irradiation of input fluence to $735 \text{ MW}/\text{cm}^2$ on the decorated system leads to very deep decrease in the transmittance as presented in Fig. 10e which is a sign of strong reverse saturable behavior. The present results of nonlinear absorption coefficient were compared with the other well-known system in Table 2 reported at same experimental setup. With increasing β for different samples considered, the difference between the valley depth and the peak height in nonlinear refraction varies. And the amplitude of the valley is almost as large as peak, referring the involvement of Kerr-type nonlinearity [52]. Thus, considering the above observation along with fact that the repetition rate of the laser that has been used in the experimental procedure is 80 MHz, the influence of thermal effects along with the electronic effects cannot be ignored.

3.5 Optical limiting behavior

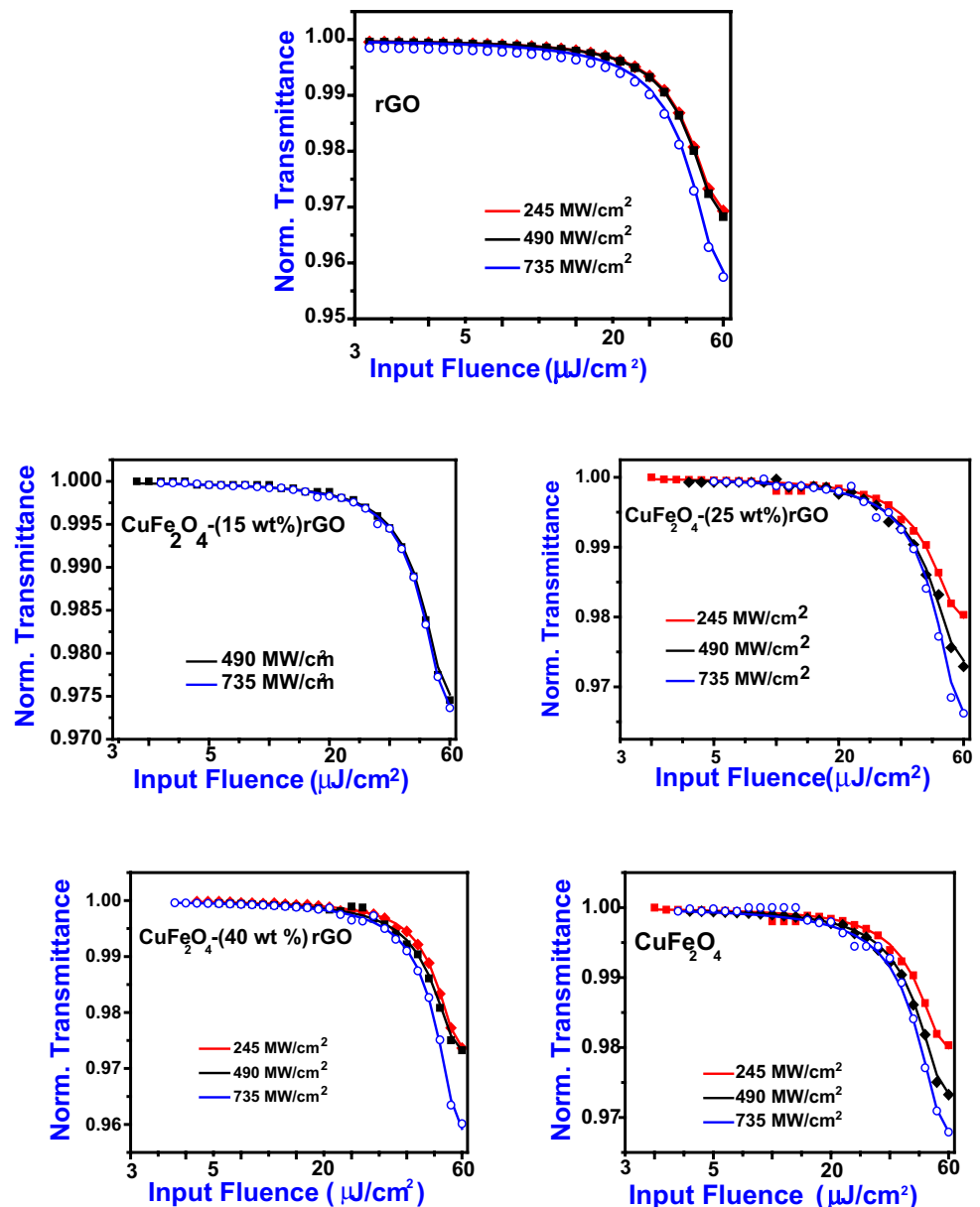
The changes in transmission of the prepared hybrids were recorded against input fluence using open aperture

Table 2 Comparison of the two-photon absorption coefficients obtained for the carbon and metal/semiconductor nanoparticles [Ti:Sapphire (~800 nm)]

Samples	Nonlinear absorption coefficient, β_{2PA} (m/W)
CdFe_2O_4 -rGO [26]	10^{-15}
ZnFe_2O_4 -rGO [48]	10^{-15}
GO and rGO [55]	10^{-13}
SiO_2 -Se [56]	10^{-15}
CuS nanoparticles [57]	10^{-15}
Ni-Ag [58]	10^{-15}
$\text{CuO}/f\text{-HEG}$ [59]	10^{-14}
Fe_2O_3 [60]	10^{-15}

Z-scan experiment. This experiment is capable of recording the variation in light fluence $[F(z)]$ for corresponding beam radius $\omega(z)$ [53, 54]. The optical limiting threshold is defined as the incident fluence at which the transmittance falls to 50% of the linear transmittance. Here all the optical limiting curves were extracted from the open aperture Z-scan data and the fluence range ($3\text{--}60 \mu\text{J}/\text{cm}^2$) is limited to the designed Z-scan geometry. As direct measurement of output with change in input intensity is not measured, the curve has the limitation of extending (or extrapolating the data) until the transmittance falls off to 50%. Hence, as an alternate approach, onset optical limiting threshold is reported which is the incident fluence at which optical limiting activity starts. The OL curve derived from the open aperture pattern demonstrates the changes in transmittance value with respect to input fluence as represented in Fig. 12. The ability to deliver ultrafast pulses with controlled energy through flexible fibers can open up a host of possibilities toward developing robust ultrafast laser microsurgery systems. It is to be noted that as short pulse lasers allow high precision microsurgery with minimal invasiveness, high repetition rate femtosecond laser is under prime consideration. Hence, femtosecond laser microsurgery has emerged strongly in tissue ablation,

Fig. 12 Intensity-dependent OL pattern of pure rGO, CuFe₂O₄-(15 wt%) rGO, CuFe₂O₄-(25 wt%) rGO, CuFe₂O₄-(40 wt%) rGO and CuFe₂O₄



studying neural injury, and cleaving microtubules which require energy pulses on the order of microjoules. Thus, the observed optical limiting of CuFe₂O₄-decorated (40 wt%) rGO with onset limiting threshold in the order of few $\mu\text{J}/\text{cm}^2$ is of potential use in biomedical applications. Here, all the samples exhibit optical limiting (due to 2PA and SDF) pattern except CuFe₂O₄-(15 wt%) rGO at 245 MW/cm² due to the existence of dominant SA process (W-pattern). As the nonlinear absorption coefficient is intensity dependent, here 2PA coefficient increases with the increase in the number of photons used for excitation. Pure rGO possesses higher 2PA coefficient compared with pure copper ferrite. At 245 MW/cm², copper ferrite possesses higher 2PA than rGO. This combination of two

extreme 2PA absorbed resulted in the variation in 2PA coefficient with change in rGO content. Among the composite, higher 2PA coefficient was observed for (40 wt%) rGO followed by (25 wt% and 15 wt%) rGO. It is interesting to note that at lower input intensity excitation rGO possesses stronger 2PA coefficient compared with the nanocomposites. Here the lowest nonlinear absorption coefficient was witnessed for (15 wt%) rGO due to the combined presence of stronger SA and weaker RSA. As witnessed in TEM, higher content of CuFe₂O₄ upon rGO has suppressed the contribution of rGO and thus possesses lower nonlinear absorption coefficient compared to pure rGO and CuFe₂O₄. However, (25 wt% and 40 wt%) rGO has a stronger 2PA coefficient than its pure counterparts. The maximum 2PA

coefficient was witnessed for CuFe_2O_4 -(40 wt%) rGO at 735 MW/cm^2 excitation due to the combined contribution of rGO and CuFe_2O_4 which is four times higher than pure rGO and CuFe_2O_4 . The presence of layer like CuFe_2O_4 nanoplatelets upon the layer rGO offers higher advantage in enhancing the nonlinear absorption coefficient. As discussed in the literature, similar tuning of NLO properties with respect to the grain size of the material was observed in CuCl nanocrystals, ZnO nanocolloids, ZnFe_2O_4 and CdO [61–63]. The decoration of copper ferrite with different concentrations upon rGO sheets with varied morphology results in acquiring tunability of NLO properties. Thus, nanoplatelet CuFe_2O_4 -(40 wt%) rGO can be potential energy-absorbing ESA-based optical limiters against Ti:Sapphire (150 fs, 800 nm and 80 MHz) laser pulses.

4 Conclusions

CuFe_2O_4 was made to anchor upon (15, 25 and 40 wt%) rGO contents by hydrothermal method where electrostatic force plays an important role in distributing and holding various sizes of particles. The decoration of CuFe_2O_4 nanostructures upon rGO nanosheets was confirmed by analyzing their XPS, XRD, FTIR, VSM, Raman, SEM, TEM and UV–Vis absorption studies. Higher content of rGO with CuFe_2O_4 nanoplatelets exhibited superior self-defocusing (NLR) and 2PA (NLA) process than other lower rGO content hybrid structure. Intensity-dependent nonlinear absorption studies showcase the following features of CuFe_2O_4 -rGO composites (1) CuFe_2O_4 -(15 wt%) rGO at lower intensity of excitation exhibits W-pattern with dominant saturable absorption behavior arising from the influence of Pauli blocking rGO, (2) CuFe_2O_4 -rGO composite exhibits near-resonant reverse saturable absorption and is ascribed to be sequential 2PA (1PA + ESA) process and (3) CuFe_2O_4 nanoplatelets decorated upon 40 wt% rGO exhibited superior self-defocusing (NLR) and 2PA (NLA) process than other lower rGO content hybrid structure due to the interaction between the layered morphologies of host and decorating molecules. The prepared CuFe_2O_4 nanoplatelet-decorated rGO hybrid layer structure provides an insight on the possible way to enhance NLO properties by anchoring layered complex oxides upon carbonaceous-layered materials.

Acknowledgements TCS acknowledges financial assistance from CSIR-India [03(1375)/16/EMR-II] and S.V acknowledges the DRDO-India financial support.

Compliance with ethical standards

Conflict of interest The author(s) declare that they have no competing interests.

References

1. Dini D, Calvete MJ, Hanack M (2016) Nonlinear optical materials for the smart filtering of optical radiation. *Chem Rev* 116:13043–13233
2. Zheng C, Chen W, Huang Y, Xiao X, Ye X (2014) Graphene oxide–noble metal (Au, Pt, and Pd) nanoparticle composites as optical limiters. *RSC Adv* 4:39697–39703
3. Mamidala V, Polavarapu L, Balapanuru J, Loh KP, Xu QH, Ji W (2010) Enhanced nonlinear optical responses in donor-acceptor ionic complexes via photo induced energy transfer. *Opt Express* 18:25928–25935
4. Liu R, Hu J, Zhu S, Lu Zhu H (2017) Synergistically enhanced optical limiting property of graphene oxide hybrid materials functionalized with pt complexes. *ACS Appl. Mater Int* 9:33029–33040
5. Krüger J, Meja P, Autric M, Kautek W (2002) Femtosecond pulse laser ablation of anodic oxide coatings on aluminium alloys with on-line acoustic observation. *Appl Surf Sci* 186:374–380
6. Debord B, Alharbi M, Vincetti L, Husakou A, Fourcade D, Hoeninger C, Mottay C, G er ome E, Benabid F (2014) Multi-meter fiber-delivery and pulse self-compression of milli-Joule femtosecond laser and fiber-aided laser-micromachining. *Opt Express* 22:10735–10746
7. Guo Q, Yao Y, Luo ZC, Qin Z, Xie G, Liu M, Kang J, Zhang S, Bi G, Liu X, Qiu J (2016) Universal near-infrared and mid-infrared optical modulation for ultrafast pulse generation enabled by colloidal plasmonic semiconductor nanocrystals. *ACS Nano* 10:9463–9469
8. Zheng X, Feng M, Zhan H (2013) Giant optical limiting effect in Ormosil gel glasses doped with graphene oxide materials. *J Mater Chem C* 1:6759–6766
9. Zhang Y, Song Y, Gan Y, Feng M, Zhan H (2015) Broadband nonlinear optical and optical limiting effects of partially unzipped carbon nanotubes. *J Mater Chem C* 3:9948–9954
10. Recatala D, Llusar R, Barlow A, Wang G, Samoc M, Humphrey MG, Guschin AL (2015) Synthesis and optical power limiting properties of heteroleptic Mo_3S_7 clusters. *Dalton Trans* 44:13163–13172
11. Song W, He C, Dong Y, Zhang W, Gao Y, Wu Y, Chen Z (2015) The effects of central metals on the photophysical and nonlinear optical properties of reduced graphene oxide–metal(III) phthalocyanine hybrids. *Phys Chem Chem Phys* 17:7149–7157
12. Qu B, Ouyang Q, Yu X, Luo W, Qi L, Chen Y (2015) Nonlinear absorption, nonlinear scattering, and optical limiting properties of MoS_2 -ZnO composite-based organic glasses. *Phys Chem Chem Phys* 17:6036–6043
13. Nuernberger P, Vogt G, Brixner T, Gerber G (2007) Femtosecond quantum control of molecular dynamics in the condensed phase. *Phys Chem Chem Phys* 9:2470–2497
14. Tang C, Zheng Q, Zhu H, Wang L, Chen SC, Ma E, Chen X (2013) Two-photon absorption and optical power limiting properties of ladder-type tetraphenylene cored chromophores with different terminal groups. *J Mater Chem C* 1:1771–1780
15. Maya EM, Snow AW, Shirk JS, Pong RG, Flom SR, Roberts GL (2003) Synthesis, aggregation behavior and nonlinear absorption properties of lead phthalocyanines substituted with siloxane chains. *J Mater Chem* 13:1603–1613
16. Kalanoor BS, Gouda L, Gottesman R, Tirosh S, Haltzi E, Zaban A, Tischler YR (2016) Third-order optical nonlinearities in organometallic methylammonium lead iodide perovskite thin films. *ACS Photonics* 3:361–370
17. Krishna MBM, Venkatramiah N, Venkatesan R, Rao DN (2012) Synthesis and structural, spectroscopic and nonlinear optical measurements of graphene oxide and its composites with metal and metal free porphyrins. *J Mater Chem* 22:3059–3068

18. Du Y, Dong N, Zhang M, Zhang Y, Luan J, Lu Y, Zhang S, Sun N, Wang J, Wang G (2016) Porphyrin–poly(arylene ether sulfone) covalently functionalized multi-walled carbon nanotubes: synthesis and enhanced broadband nonlinear optical properties. *RSC Adv* 6:75530–75540
19. Sanusi K, Stone JM, Nyokong T (2015) Nonlinear optical behaviour of indium-phthalocyanine tethered to magnetite or silica nanoparticles. *New J Chem* 39:1665–1677
20. Tolbin AY, Savelyev MS, Gerasimenko AY, Tomilova L, Zefirov NS (2016) Thermally stable J-type phthalocyanine dimers as new non-linear absorbers for low-threshold optical limiters. *Phys Chem Chem Phys* 18:15964–15971
21. Zhang XL, Zhao X, Liu ZB, Shi S, Zhou WY, Tian JG, Xu YF, Chen YS (2011) Nonlinear optical and optical limiting properties of graphene oxide–Fe₃O₄ hybrid material. *J Opt* 13:075202
22. Saravanan M, Sabari Girisun TC (2017) Enhanced nonlinear optical absorption and optical limiting properties of superparamagnetic spinel zinc ferrite decorated reduced graphene oxide nanostructures. *Appl Surf Sci* 392:904–911
23. Kavitha MK, John H, Gopinath P, Philip R (2013) Synthesis of reduced graphene oxide–ZnO hybrid with enhanced optical limiting properties. *J Mater Chem C* 1:3669–3676
24. Wang A, Yu W, Fang Y, Song Y, Jia D, Long L, Cifuentes MP, Humphrey MG, Zhang C (2015) Facile hydrothermal synthesis and optical limiting properties of TiO₂-reduced graphene oxide nanocomposites. *Carbon* 89:130–141
25. Muruganandi G, Saravanan M, Vinitha G, Raj MJ, Sabari Girisun TC (2018) Barium borate nanorod decorated reduced graphene oxide for optical power limiting applications. *Opt Mater* 75:612–618
26. Al-Asadi AS, Hassan QM, Abdulkader AF, Mohammed MH, Bakr H, Emshary CA (2019) Formation of graphene nanosheets/epoxy resin composite and study its structural, morphological and nonlinear optical properties. *Opt Mater* 89:460–467
27. Abdulkader AF, Hassan QMA, Al-Asadi AS, Bakr H, Sultan HA, Emshary CA (2018) Linear, nonlinear and optical limiting properties of carbon black in epoxy resin. *Optik* 160:100–108
28. Bourlinos AB, Bakandritsos A, Liaros N, Couris S, Safarova K, Otyepka M, Zbořil R (2012) Water dispersible functionalized graphene fluoride with significant nonlinear optical response. *Chem Phys Lett* 543:101–105
29. Feng M, Zhan H, Chen Y (2010) Nonlinear optical and optical limiting properties of graphene families. *Appl Phys Lett* 96:033107
30. Jiang XF, Polavarapu L, Neo ST, Venkatesan T, Xu Q H (2012) Graphene oxides as tunable broadband nonlinear optical materials for femtosecond laser pulses. *J Phys Chem Lett* 3:785–790
31. Kadhum AJ, Hussein NA, Hassan QM, Sultan HA, Al-Asadi AS, Emshary CA (2018) Investigating the nonlinear behavior of cobalt(II) phthalocyanine using visible CW laser beam. *Optik* 157:540–550
32. Liaros N, Koudoumas E, Couris S (2014) Broadband near infrared optical power limiting of few layered graphene oxides. *Appl Phys Lett* 104:191112
33. Nalla V, Polavarapu L, Manga KK, Goh BM, Loh KP, Xu QH, Ji W (2010) Transient photoconductivity and femtosecond nonlinear optical properties of a conjugated polymer–graphene oxide composite. *Nanotech* 21:415203
34. Zhang H, Virally S, Bao Q, Ping LK, Massar S, Godbout N, Kockaert P (2012) Z-scan measurement of the nonlinear refractive index of graphene. *Opt Lett* 37:1856–1858
35. Saravanan M, Sabari Girisun TC, Venugopal Rao S (2017) Superparamagnetic and unusual nonlinear absorption switching behavior of an in situ decorated CdFe₂O₄-rGO nanocomposite. *J Mater Chem C* 5:9929–9942
36. Wesner DA, Mertin M, Lupp F, Kreutz EW (1996) Cleaning of copper traces on circuit boards with excimer laser radiation. *Appl Surf Sci* 96:479–483
37. Fu Y, Chen Q, He M, Wan Y, Sun X, Xia H, Wang X (2012) Copper ferrite-graphene hybrid: a multifunctional heteroarchitecture for photocatalysis and energy storage. *Ind Eng Chem Res* 51:1700–17109
38. Faungnawakij K, Kikuchi R, Shimoda N, Fukunaga T, Eguchi K (2008) Effect of thermal treatment on activity and durability of CuFe₂O₄-Al₂O₃ composite catalysts for steam reforming of dimethyl ether. *Angew Chem* 120:9454–9457
39. Anand B, Kaniyoor A, Sai SSS, Philip R, Ramaprabhu S (2013) Enhanced optical limiting in functionalized hydrogen exfoliated graphene and its metal hybrids. *J Mater Chem C* 1:2773–2780
40. Meidanchi A, Akhavan O (2014) Superparamagnetic zinc ferrite spinel–graphene nanostructures for fast wastewater purification. *Carbon* 69:230–238
41. Eswaraiiah V, Aravind SSJ, Ramaprabhu S (2011) Top down method for synthesis of highly conducting graphene by exfoliation of graphite oxide using focused solar radiation. *J Mater Chem* 21:6800–6803
42. Kumar A, Rout L, Achary LSK, Dhaka RS, Dash P (2017) Greener route for synthesis of aryl and alkyl-14H-dibenzo [a]j xanthenes using graphene oxide-copper ferrite nanocomposite as a recyclable heterogeneous catalyst. *Sci Rep* 7:42975
43. Matzen S, Moussy JB, Mattana R, Bouzehouane K, Deranlot C, Petroff F, Cezar J C, Arrio MA, Sainctavit P, Gatel C, Warot-Fonrose B (2011) Epitaxial growth and ferrimagnetic behavior of MnFe₂O₄ (111) ultrathin layers for room-temperature spin filtering. *Phys Rev B* 83:184402
44. Kaniyoor A, Baby TT, Ramaprabhu S (2010) Graphene synthesis via hydrogen induced low temperature exfoliation of graphite oxide. *J Mater Chem* 20:8467–8469
45. Kumar D, Narayan J, Kvit AV, Sharma AK, Sankar J (2001) High coercivity and superparamagnetic behavior of nanocrystalline iron particles in alumina matrix. *J Magn Magn Mater* 232:161–167
46. Su J, Cao M, Ren L, Hu C (2011) Fe₃O₄-graphene nanocomposites with improved lithium storage and magnetism properties. *J Phys Chem C* 115:14469–14477
47. Sheik-Bahae M, Said AA, Wei TH, Hagan DJ, Van Stryland EW (1990) Sensitive measurement of optical nonlinearities using a single beam. *IEEE J Quan Elect* 26:760–769
48. Saravanan M, Sabari Girisun TC, Vinitha G, Rao SV (2016) Improved third-order optical nonlinearity and optical limiting behaviour of (nanospindle and nanosphere) zinc ferrite decorated reduced graphene oxide under continuous and ultrafast laser excitation. *RSC Adv* 6:91083–91092
49. Ramakanth S, Hamad S, Venugopal Rao S, James Raju KC (2015) Magnetic and nonlinear optical properties of BaTiO₃ nanoparticles. *AIP Adv* 5:057139
50. Torres TC, Bornacelli J, Can Uc B, Silva Pereyra HG, Rodríguez Fernández L, Avalos-Borja M, Labrada Delgado GJ, Cheang Wong JC, Rangel Rojo R, Oliver A (2018) Coexistence of two-photon absorption and saturable absorption in ion-implanted platinum nanoparticles in silica plates. *JOSA B* 35:1295–1300
51. Stewart AF, Bass M (1980) Intensity-dependent absorption in semiconductors. *Appl Phys Lett* 37:1040–1043
52. Palfalvi L, Hebling J (2004) Z-scan study of the thermo-optical effect. *Appl Phys B* 78:775–780
53. SheikBahae M, Ali Said A, Hagan DJ, Soileau MJ, Van Stryland W (1991) Nonlinear refraction and optical limiting in thick media. *Opt Eng* 30:1228–1235
54. Saravanan M, Sabari Girisun TC (2015) Nonlinear optical absorption and optical limiting properties of cadmium ferrite. *Mater Chem Phys* 160:413–419

55. Perumbilavil S, Sankar P, PriyaRose T, Philip R (2015) White light Z-scan measurements of ultrafast optical nonlinearity in reduced graphene oxide nanosheets in the 400–700 nm region. *Appl Phys Lett* 107:051104
56. Mary KA, Unnikrishnan NV, Philip R (2015) Cubic to amorphous transformation of Se in silica with improved ultrafast optical nonlinearity. *RSC Adv* 5:14034–14041
57. Mary KA, Unnikrishnan NV, Philip R (2014) Role of surface states and defects in the ultrafast nonlinear optical properties of CuS quantum dots. *APL Mater* 2:076104
58. Sridharan K, Endo T, Cho SG, Kim J, Park TJ, Philip R (2013) Single step synthesis and optical limiting properties of Ni–Ag and Fe–Ag bimetallic nanoparticles. *Opt Mater* 35:860–867
59. Anand B, Kaniyoor A, Swain D, Baby TT, Rao SV, Sai SSS, Ramaprabhu S, Philip R (2014) Enhanced optical limiting and carrier dynamics in metal oxide–hydrogen exfoliated graphene hybrids. *J Mater Chem C* 2:10116–10123
60. Thomas P, Sreekanth P, Abraham KE (2015) Nanosecond and ultrafast optical power limiting in luminescent Fe₂O₃ hexagonal nanomorphotype. *J Appl Phys* 117:053103
61. Irimpan L, Nampoorei VPN, Radhakrishnan P, Krishnan B, Deepthy A (2008) Size-dependent enhancement of nonlinear optical properties in nanocolloids of ZnO. *J Appl Phys* 103:033105
62. Thomas JJ, Krishnan S, Sridharan K, Philip R, Kalarikkal N (2012) A comparative study on the optical limiting properties of different nano spinel ferrites with Z-scan technique. *Mater Res Bull* 47:1855–1860
63. Thomas P, Sreekanth P, Philip R, Abraham KE (2015) Morphology dependent nanosecond and ultrafast optical power limiting of CdO nanomorphotypes. *RSC Adv* 5:35017–35025

Publisher's Note Springer Nature remains neutral with regard to jurisdictional claims in published maps and institutional affiliations.